

Large linear non-saturating magnetoresistance and high mobility in ferromagnetic MnBi

Yangkun He ¹✉, Jacob Gayles ^{1,2}, Mengyu Yao ¹, Toni Helm ^{1,3}, Tommy Reimann ³, Vladimir N. Strocov ⁴, Walter Schnelle¹, Michael Nicklas ¹, Yan Sun ¹, Gerhard H. Fecher¹ & Claudia Felser¹

A large non-saturating magnetoresistance has been observed in several nonmagnetic topological Weyl semi-metals with high mobility of charge carriers at the Fermi energy. However, ferromagnetic systems rarely display a large magnetoresistance because of localized electrons in heavy d bands with a low Fermi velocity. Here, we report a large linear non-saturating magnetoresistance and high mobility in ferromagnetic MnBi. MnBi, unlike conventional ferromagnets, exhibits a large linear non-saturating magnetoresistance of 5000% under a pulsed field of 70 T. The electrons and holes' mobilities are both $5000 \text{ cm}^2 \text{ V}^{-1} \text{ s}^{-1}$ at 2 K, which are one of the highest for ferromagnetic materials. These phenomena are due to the spin-polarised Bi $6p$ band's sharp dispersion with a small effective mass. Our study provides an approach to achieve high mobility in ferromagnetic systems with a high Curie temperature, which is advantageous for topological spintronics.

¹Max-Planck-Institute for Chemical Physics of Solids, Dresden, Germany. ²Department of Physics, University of South Florida, Tampa, FL, USA. ³Dresden High Magnetic Field Laboratory (HLD-EMFL), Helmholtz-Zentrum Dresden-Rossendorf, Dresden, Germany. ⁴Swiss Light Source, Paul Scherrer Institut, Villigen, Switzerland. ✉email: yangkun.he@cpfs.mpg.de

Weyl fermions, massless chiral quasiparticles in the momentum space, host some of the most intriguing transport phenomena, such as the anomalous Hall effect (AHE)¹, anomalous Nernst effect², (quantum) oscillations^{3,4}, or a large positive transverse magnetoresistance (MR)^{5,6}. Nonmagnetic examples of topological Weyl semi-metals, such as TaAs⁷, NbP⁶, and WTe₂⁵, have been reported with a giant positive MR of more than 10⁵% at low temperatures. Its origin lies in the massless Weyl states associated to the linear band crossings at the Fermi energy and a high Fermi velocity. Magnetic topological semimetals allow for the manipulation of the Fermi surface topology by external electromagnetic fields and are therefore fundamental in topological spintronics research.

Only a few examples of ferromagnetic topological materials, such as Fe₃Sn₂⁸, Co₃Sn₂S₂¹, and Co₂MnGa^{2,9}, have been reported to exhibit a weakly positive MR of 20–30%. Although these values are much larger than those of their non-topological ferromagnetic relatives, they are significantly lower than those of the leading nonmagnetic examples (see Fig. 1e). This is because the mobility μ of ferromagnetic Weyl semi-metals is still considerably less than 10³ cm² V⁻¹ s⁻¹, due to both electron and spin scattering. Only in the case of higher mobilities is the criterion $\mu B > 1$ fulfilled (B is the applied magnetic field), enabling the observation of quantum effects and thus a large linear non-saturating MR¹⁰.

Giant MR has attracted a broad interest because of its theoretical aspects and its commercial applications, such as spin-valve sensors¹¹ and hard disc read/write heads¹². In ordinary non-magnetic metals, the MR is usually a small value of only a few percent. In ferromagnetic materials, which are metals in most cases, the MR is generally small and negative (inset of Fig. 1e) owing to spin disorder scattering. Considerable efforts have been made to find new FM materials with a large MR. A giant MR of 150% was observed in Fe–Cr thin-film heterostructures at 4.2 K, associated with spin-flip scattering¹³. In some ferromagnetic semiconductors, such as HgCr₂Se₄¹⁴, LaMnO₃¹⁵, and EuO¹⁶, a colossal MR was reported near the Curie temperature (T_c), which is due to a magnetic-field-induced semiconductor-to-metal phase transition. However, this phase transition requires a large magnetic field and is usually accompanied by a large hysteresis¹⁷. Yet,

Weyl semimetals have more simplistic and predictable electronic structures. Due to the topology—the electronic structure suppresses backscattering and spin scattering which leads to some of the largest MR values found.

Herein, we report the transport properties of single-crystal ferromagnetic MnBi. A large linear non-saturating MR, defined as the ratio of the change in resistance $\rho(B) - \rho(0)$ in response to an applied magnetic field $[\rho(B) - \rho(0)]/\rho(0)$. Furthermore, we find one of the largest mobilities in ferromagnetic materials. These phenomena are due to the linear dispersion of the $6p$ band at the Fermi energy with a small effective mass as confirmed from state-of-the-art first-principle calculations, as well as angle-resolved photoemission spectroscopy (ARPES) and Shubnikov–de Haas (SdH) oscillations experiments on single crystals. In this sense, MnBi with an MR comparable to nonmagnetic semimetals is unique in comparison to the topological ferromagnetic counterparts. And a giant MR single crystal device that is tunable purely by the magnetic moment can have far-reaching implications for spintronic devices.

Results

Crystal and magnetic structure. MnBi crystallizes in a NiAs-type crystal structure with the space group $P6_3/mmc$ (No. 194). It consists of alternating Mn and Bi layers, as shown in Fig. 1a. The lattice constants are obtained as $a = 4.2876(5)$ Å and $c = 6.1154(5)$ Å, based on X-ray diffraction results. Known as a room-temperature hard magnet with a large maximum energy product¹⁸, MnBi exhibits a large moment of 3.94 μ_B per Mn atom and a high Curie temperature ($T_c > 630$ K)¹⁹. Below the spin-reorientation transition temperature $T_{SR1} = 137$ K, the moment gradually rotates away from the c -axis upon cooling²⁰ and abruptly flips close to the ab -plane¹⁹ at $T_{SR2} = 87$ K.

The temperature-dependent longitudinal resistivity of MnBi is shown in Fig. 1b. The high-quality single crystal grown via the flux method shows a metallic behavior with a sizeable residual-resistivity ratio (RRR) of 100 (see also Supplementary Fig. 1 in the supplemental material). This indicates the high quality of the single crystal and very high mobility, suppressed by phonon

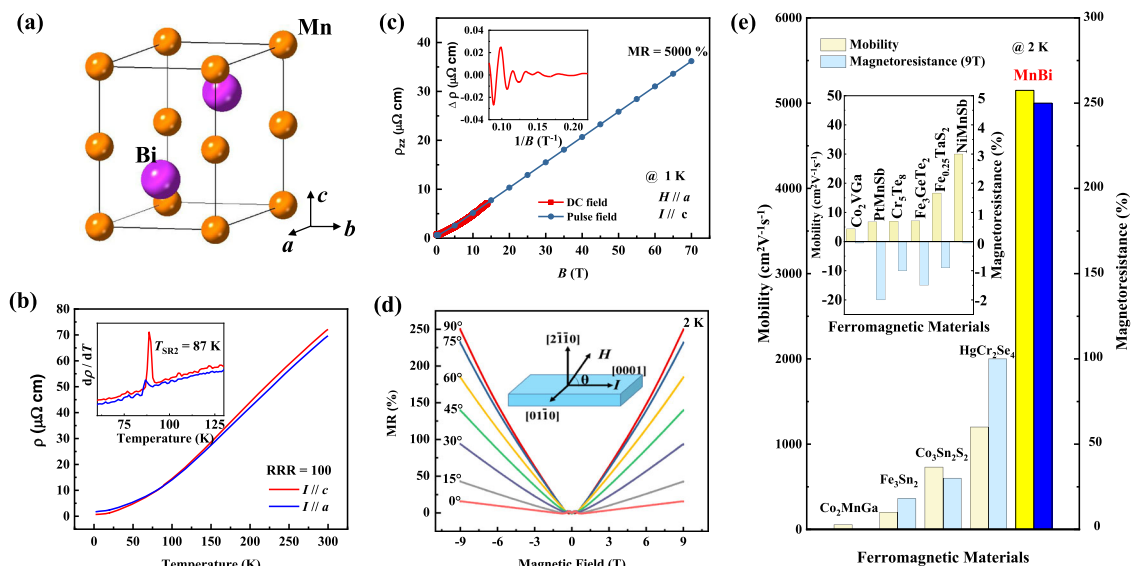


Fig. 1 Crystal structure and measured resistivity of MnBi. **a** The crystal structure of MnBi in space group $P6_3/mmc$. **b** Longitudinal resistivity along with the c - and a -axes. The inset shows a kink for $d\rho/dT$ at T_{SR2} . **c** Non-saturating linear MR under a pulse-field of 70 T at 1 K. The inset shows the SdH oscillations obtained from the resistivity data below 14 T under a DC magnetic field. **d** Angular-dependent MR at 2 K. **e** Comparison of its MR and high mobility with those of other ferromagnetic materials. Data for other ferromagnetic materials come from refs. 1,8,9,41–45. The inset shows the low mobility and negative MR for ordinary ferromagnetic materials.

scattering during heating²¹. The longitudinal resistivity ρ decreases to $0.69 \mu\Omega \text{ cm}$ along the c -axis and $1.7 \mu\Omega \text{ cm}$ at 2 K along the a -axis. An additional kink in the differential resistivity at a T_{SR2} of 87 K is shown in the inset. Strictly speaking, the crystal structure is orthorhombic below T_{SR2} due to the magnetostriction¹⁹, but this small distortion is ignored in the analysis.

Magnetoresistance. A non-saturating linear MR of 5000% under a pulsed-field of 70 T at 1 K is shown in Fig. 1c. The data measured under a direct current (DC) magnetic field of 14 T are also shown for comparison. The Shubnikov–de Haas oscillations were observed with a single frequency at 23 T by subtracting a cubic polynomial from the resistivity data below 14 T, as shown in the inset. The detailed data are shown in Supplementary Fig. 2 of the supplement. The MR is strongly angular dependent, as shown in Fig. 1d. The MR decreases from 250 to 15% at 9 T when the field changes from perpendicular to parallel to the current.

With increasing temperature, the MR becomes less evident in Fig. 2a, and it has a small negative value above 90 K, just as a normal ferromagnet (see Fig. 2b). The non-saturating MR reveals a two-charge carrier behavior at low temperatures, where holes and electrons have almost the same density⁵. The individual quantum levels associated with the electron orbits should be distinct to realize this phenomenon¹⁰. In other words, our results indicate that there exists an approximately linear energy spectrum in the band structure and carriers of a very low effective mass.

The MR was also measured under different fields and current directions. It is positive at low temperatures, independent of the field and current directions. The MR is the largest when $I \parallel c$, and it is lower when the current is in the ab plane. The larger and non-saturated MR when $I \parallel c$ may result from the more effective compensation of electrons and holes. Above 90 K, the MR is negative during magnetization when $H \parallel a$ and $I \parallel c$ or when $H \parallel c$ and $I \parallel a$ (Fig. 2b, f), whereas it is positive when both the current and field are in-plane (Fig. 2d). Notably, a butterfly shape is observed in Fig. 2f, owing to the hysteresis at high temperatures when MnBi becomes a hard magnet in a micron-sized single crystal.

Hall resistivity and two-charge-carrier behavior. The Hall resistivity ρ_{H} at different temperatures is shown in Fig. 3a when the field is parallel to the a -axis, and the current is parallel to the c -axis. At 2 K, the curve further confirms the two-charge-carrier behavior at low temperatures. Note that the curves correspond to the ordinary Hall effect rather than the AHE. The reason for rejecting an anomalous contribution is that the magnetization, which determines the AHE field dependence, is already saturated at 0.5 T. In contrast, the observed Hall signal does not become saturated, as shown in the inset.

There is no suitable two-charge-carrier model to fit the MR of a ferromagnetic material because the magnetization process removes the domain walls and decreases the domain wall scattering. This leads to an additional negative MR, as shown in Fig. 2a when the field is less than 0.5 T. However, for the Hall signal, the anomalous Hall resistivity is zero without a magnetic field owing to:

1. the negligible hysteresis due to the easy plane magnetic structure at a low temperature and
2. the intrinsic anomalous Hall resistivity that is two orders lower than the normal Hall resistivity at saturation because of the extremely small longitudinal ρ ($\sigma_{\text{H}} = -\rho_{\text{H}}/\rho^2$, where σ_{H} is the intrinsic Hall conductivity deduced from the slope in Fig. 3d), which is similar to that of pure Fe²² and Gd²³.

Therefore, the AHE is negligible compared with the ordinary Hall effect at low temperatures. We fit the two-charge-carrier model using Hall resistivity as follows:

$$\rho_{\text{H}} = -\frac{1(n\mu^2 - p\mu'^2) - (p - n)\mu^2\mu'^2 B^2}{e(n\mu + p\mu')^2 + [(p - n)\mu\mu' B]^2} B \quad (1)$$

where p and n are the charge carrier densities for holes and electrons, respectively, and μ' and μ are the mobilities of holes and electrons. The fitted curve at 2 K is shown in the inset of Fig. 3a. The densities of both holes and electrons are almost the same at approximately $9 \times 10^{20} \text{ cm}^{-3}$ (0.02 hole/electron per formula), and they are temperature independent, consistent with previously reported values²⁴. The mobilities of both the charge carriers are high, i.e., approximately $5000 \text{ cm}^2 \text{ V}^{-1} \text{ s}^{-1}$ at 2 K. This value

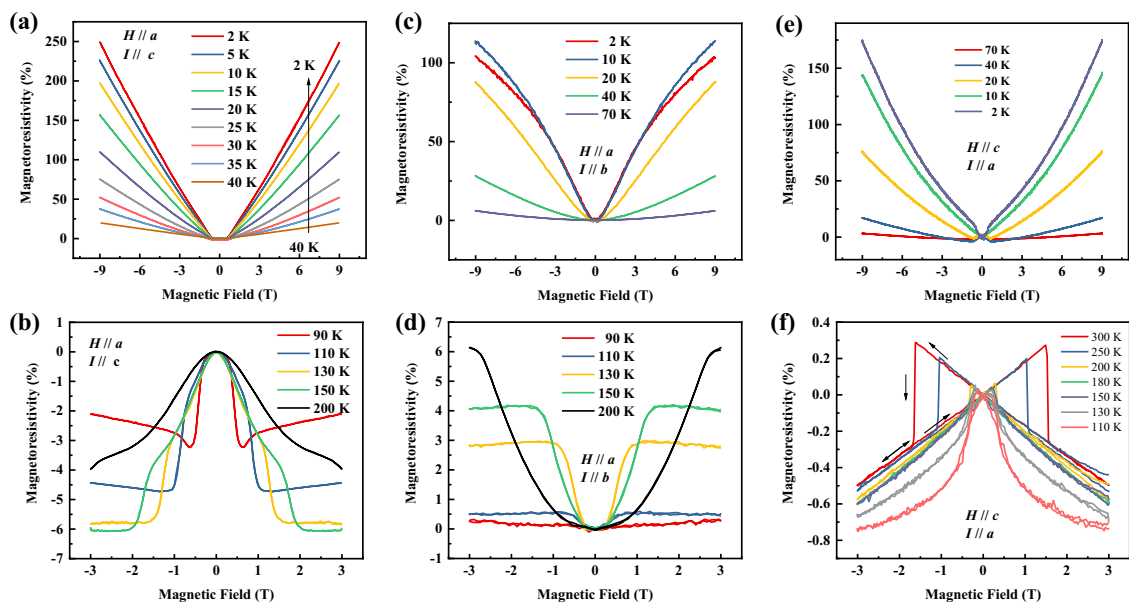


Fig. 2 MR under different fields and current directions. **a, b** $H \parallel a$ and $I \parallel c$. **c, d** $H \parallel a$ and $I \parallel b$. **e, f** $H \parallel c$ and $I \parallel a$. The data in (e) and (f) are obtained using a micron-sized single crystal cut using the focused ion beam technique because of the bar shape of the crystal, whereas the data in a-d are obtained by using bulk single crystals.

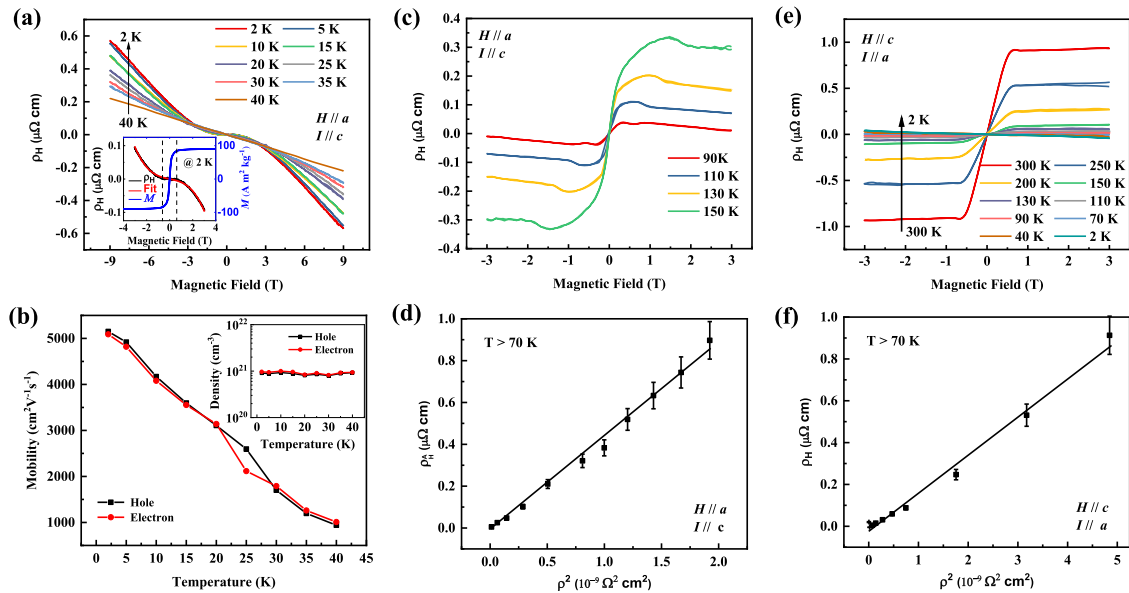


Fig. 3 Hall effect of MnBi. **a–d** for $H//a$ and $I//c$, and **e–f** for $H//c$ and $I//a$. **a** Hall effect between 2 and 40 K with typical two-charge-carrier features. The inset shows the magnetization and fits using a two-charge-carrier model. The field-dependent AHE, proportional to the magnetization, is saturated at approximately 0.5 T shown by dashed lines. In contrast, the Hall resistivity slope still changes under a magnetic field greater than 4 T due to the different charge carriers. **b**, Mobility and charge carrier density (inset) at different temperatures. **c**, **e** Hall resistivity at different temperatures. **d**, **f** Anomalous Hall resistivity versus the longitudinal resistivity square. The slopes of these curves are the intrinsic anomalous Hall conductivity. The error bar due to the uncertainty of the geometry of the sample is estimated as 10%.

decreases with increasing temperature to $900 \text{ cm}^2 \text{ V}^{-1} \text{ s}^{-1}$ at 40 K. Fitting with three or more charge carrier models would be more accurate because of the complicated band structure at the Fermi energy, but the conclusion of the high mobility does not change.

We compared the MR and mobility of MnBi with those of other ferromagnetic materials at 2 K, as shown in Fig. 1e. Ordinary ferromagnets usually have a negative MR of a few percent and rather low mobility ($< 50 \text{ cm}^2 \text{ V}^{-1} \text{ s}^{-1}$) due to the large effective mass of d electrons and spin scattering. Topological materials show a large positive MR with high mobilities due to the topological bands and small effective masses. MnBi has the highest mobility among ferromagnetic materials.

At temperatures above 90 K, the AHE becomes noticeable, as shown in Fig. 3c, because the longitudinal resistivity is much larger. At high temperatures, the conductivity is in the range of 10^4 – $10^6 \Omega^{-1} \text{ cm}^{-1}$, where the intrinsic Berry phase dominates the Hall effect²⁵. The anomalous Hall resistivity versus the longitudinal resistivity square is shown in Fig. 3d. A linear fit provides an intrinsic σ_H of $-450 \Omega^{-1} \text{ cm}^{-1}$, comparable to $-640 \Omega^{-1} \text{ cm}^{-1}$ from the Berry curvature calculation (see Fig. 4b). More information about the Hall can be found in Supplementary Fig. 3. The anomalous Hall resistivity when the field is along the c -axis and current long the a -axis is shown in Fig. 3e. The intrinsic σ_H is smaller as $-187 \Omega^{-1} \text{ cm}^{-1}$, as shown in Fig. 3f.

Band structure. The calculated band structure with a moment parallel to the a -axis is shown in Fig. 4a. It presents a typical semi-metallic band structure with both electron and hole pockets. The band structure was confirmed using ARPES. Based on the photon energy (h) dependent measurement, $k_z = 0$ plane can be reached by using photon energy $h\nu = 400 \text{ eV}$. The Fermi surface in the plane perpendicular to the z -direction when $k_z = 0$ exhibits a flower-like texture, as shown in Fig. 4e. The calculated Fermi surface is shown in Fig. 4f and Supplementary Fig. 4. A series of hole pockets located at the Γ point is surrounded by six electron

pockets located at the M points, confirming the two-charge-carrier behavior in the transport measurements. Note that the X-ray beam spot's diameter is approximately $100 \mu\text{m}$, which is much larger than the domain size of bulk MnBi at low temperatures (typically 10^0 – $10^1 \mu\text{m}$). Therefore, the data are average values for the Fermi surfaces from different domains with the in-plane magnetic spin structure, showing a six-fold symmetry.

The ARPES intensity plots along M_1 – Γ – M_4 and M_2 – M_3 are shown in Fig. 4c, d and Supplementary Fig. 5. The k_z -dispersion is also shown in Supplementary Fig. 6. The band structure was calculated by considering a rigid energy shift overlapped with the ARPES spectrum. This calculation is consistent with the experimental data. The observed electron bands are fitted with a parabola. Consequently, we find that the Fermi velocity is approximately 3.6 – $10.2 \text{ eV}\text{\AA}$. The effective mass is in the range of 0.42 – $2.54 m_0$ (m_0 is the mass of an electron) due to the dispersive band structure around the Fermi energy E_F . The detailed fitting is shown in Supplementary Fig. 7. This result confirms the previous calculation²⁶, and the value is smaller than 0.98 – $3.9 m_0$ in the magnetic Weyl semi-metal $\text{Co}_3\text{Sn}_2\text{S}_2$ ¹. These bands are responsible for the low-frequency oscillations shown in the inset of Fig. 1c²⁶. According to the relationship between μ and m_0 , which can be expressed as $\mu = \frac{q}{m_0} \tau$, where q is the elementary charge and τ is the average scattering time; the low effective mass is the origin of the high transport mobility in MnBi.

While the conventional characteristic of larger mobility is seen from trivial holes and electrons ($E \sim p^2$), here the unique contribution of the linear dispersion of the topologically non-trivial bands ($E \sim p^1$) are complementary to the electron–hole pockets. Furthermore, the unique case topological character of the bands in magnetic MnBi, as shown in Supplementary Fig. 5, allow for the reduction of backscattering which would only increase the mobility. While the linear crossing is present in other ferromagnetic topological metals, MnBi is “special” in that the Bi $6p$ bands contribute to the magnetism²⁷ in addition to the complementary connection between the electron–hole

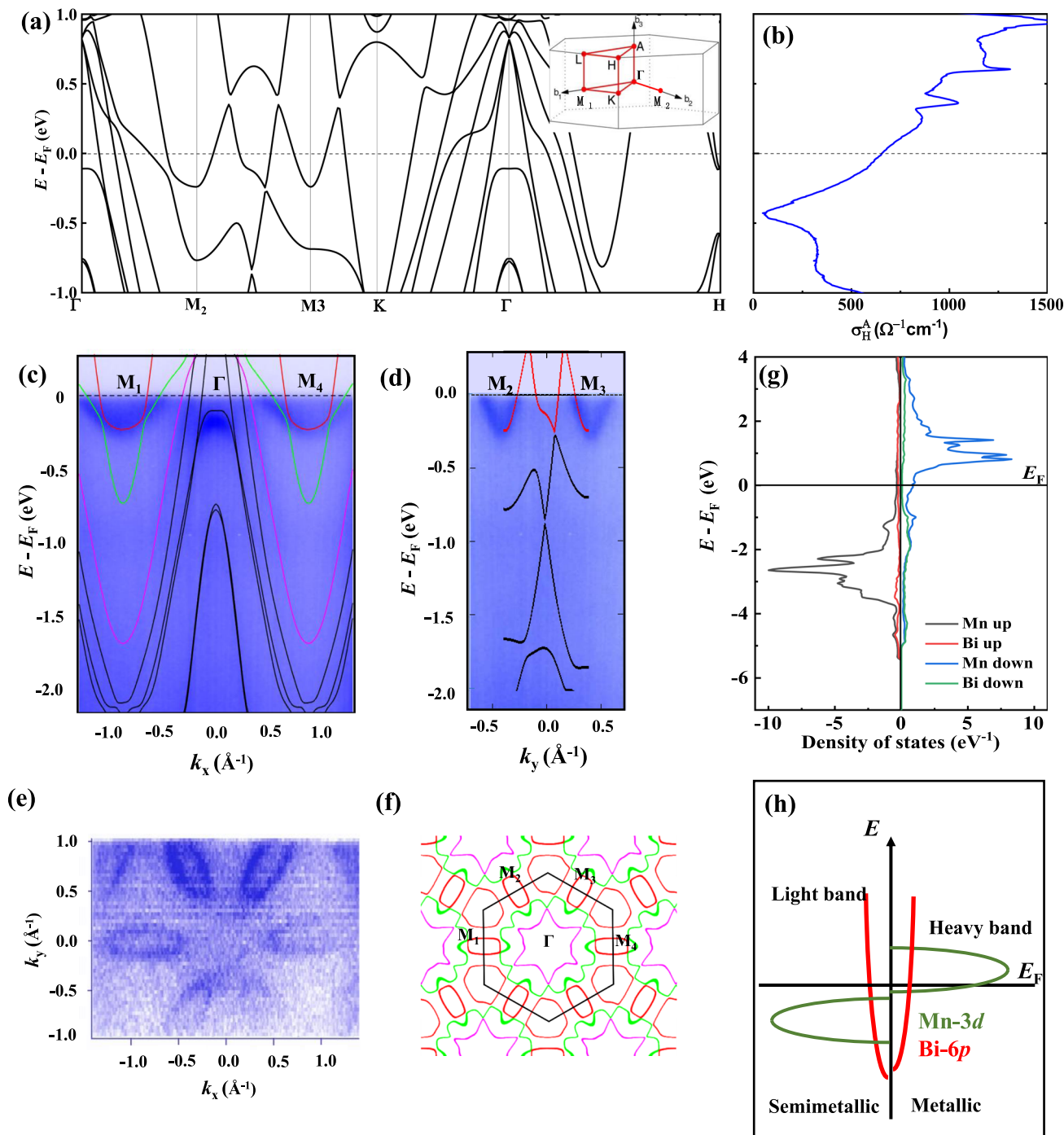


Fig. 4 Electronic structure of MnBi. **a** Band structure with the magnetic moment parallel to the *a*-axis with spin-orbit coupling. The inset shows the Brillouin zone of the hexagonal structure. **b** Intrinsic anomalous Hall conductivity calculated from the Berry curvature from the band structure. **c** ARPES intensity plot along with the M_1 - Γ - M_4 direction with calculated bands overlaid on top. **d** ARPES intensity plot along with the M_2 - M_3 direction with calculated bands overlaid on top. **e** Fermi surface map of MnBi at $k_z = 0$, which represents the photoemission intensity integrated over a small energy window $E = E_F \pm 20$ meV around the Fermi level. **f** Calculated Fermi surface at $k_z = 0$. **g** Density of states. **h** Schematic view of the density of states, showing light semi-metallic bands in the spin-up channel and heavy metal bands in the spin-down channel.

compensation and the topological bands. The linear crossing leads to a special case of electron-hole compensation that shows to drastically enhances the mobility of magnetic systems.

Discussion

The high mobility can also be explained by states' density, as shown in Fig. 4g, h. According to our calculation and previous

reports^{26,28}, the spin moment for Mn is 3.7 μ_B , and the orbital moment is 0.2 μ_B . In contrast, the rest moment of approximately 0.1 μ_B is contributed by the polarized Bi. Whereas Mn 3*d* electrons are more localized and do not conduct electricity well, 6*p* electrons in Bi are delocalized, thus dominating the transport properties. Meanwhile, the spin polarization of MnBi is high²⁹, indicating that there is no large Mn 3*d* density of states at the Fermi energy^{26,28} in the spin-up channel, with the fully occupied

Mn $3d^5$ approximately 2 eV below the Fermi energy. All the electrons mentioned above and magnetic structures indicate MnBi as a magnetic “Bi” from transport properties.

Bi and several of its alloys and compounds, such as Bi–Sb³⁰, LaBi³¹, GdPtBi³², and Bi₂Te₃³³, are topological materials with high mobility, owing to the highly delocalized $6p$ electrons of Bi and its high spin–orbital coupling. In MnBi, the Bi $6p$ orbital is strongly hybridized with Mn $3d$ electrons, confirmed by the induced magnetism in Bi, as proven using X-ray magnetic circular dichroism²⁷. Therefore, the transport properties are dominated by the magnetic Bi $6p$ electrons. Despite the record mobility and large intrinsic anomalous Hall conductivity, MnBi also shows a large anomalous Nernst effect due to the intrinsic Berry curvature³⁴, which further confirms the combination of magnetism and topological band structure and the novelty of adding Mn and Bi together.

Mn is often used as a magnetic element in topological materials, such as Mn₃Sn³⁵ and EuMnBi₂³⁶, where a large AHE and quantum Hall effect have been realized. Unfortunately, the Mn atoms’ magnetic moments in these materials are anti-ferromagnetically coupled, either non-collinearly or collinearly. To achieve ferromagnetism for realizing the quantum AHE, the thickness of the two-dimensional anti-ferromagnet MnBi₂Te₄ must be reduced to a few nanometers so that an even number of layers can achieve ferrimagnetism³⁷. So far, ferromagnetic Weyl semi-metals are mainly Co-based, e.g., Co₂MnGa^{2,9} and Co₃Sn₂S₂¹, with small moments of 1.33 (which is also mainly provided by Mn) and 0.3 μ_B per magnetic atom, respectively. MnBi has a relatively large magnetic moment of 3.94 μ_B /Mn, one of the largest in a rare-earth-free ferromagnetic material. A large moment can be easily detected and influenced by the magnetic field. The simple crystal structure of alternative Mn and Bi layers, combined with a high Curie temperature (630 K), makes MnBi a good candidate for thin films for applications in future spintronics as a sensor for detecting temperature, field, and orientation.

In summary, MnBi exhibits abnormal transport properties. Its high mobility of 5000 $\text{cm}^2 \text{V}^{-1} \text{s}^{-1}$ at 2 K is the highest for ferromagnetic materials. A positive linear MR of 5000% is not saturated up to 70 T. The two-charge-carrier behavior with a relatively low density, together with an intrinsic σ_H of 450 $\Omega^{-1} \text{cm}^{-1}$, indicates a topological band structure in the momentum space, making MnBi similar to magnetized Bi. The effective mass is as small as 0.42 m_0 . The linear MR is strongly temperature-, field-, and orientation-dependent, indicating that MnBi might be suitable for use as a sensor in future spintronics.

Methods

Single crystal growth. High-quality MnBi crystals were grown using the flux method. Accordingly, 0.36 g of Mn (99.95%) and 15 g of Bi (99.9999%) pieces were ground lightly, mixed in an alumina crucible, and sealed in an evacuated quartz tube. The tube was heated to 1273 K for 20 h, held for 24 h, cooled to 653 K in 10 h, and then slowly cooled to 548 K within 170 h before centrifugation. Short bar-like single crystals of size a few millimeters were formed. The crystals were carefully polished to remove any remaining Bi flux from the surface. Subsequently, they were examined using scanning electron microscopy to confirm the clean surface. MnBi is not stable in air, and the crystals will be partly oxidized after being exposed to air overnight. Therefore, single crystals were used for the experiments immediately after cleaning the surface.

MnBi single crystals were confirmed with a NiAs-type crystal structure via powder X-ray diffraction using a monochromator’s Cu K α radiation. The composition was characterized using energy-dispersive X-ray (EDX) analysis to be Mn_{49.2}Bi_{50.8} (uncertainty in EDX is 1%). The orientation of the single crystals was confirmed using the Laue method.

Magnetization. The magnetization measurements were conducted on single crystals with the magnetic field applied along either the a - or c -axis using a vibrating sample magnetometer (MPMS 3, Quantum Design). The sample was carefully immobilized with glue considering the strong torque. At 300 K, MnBi is a

good hard magnet with large magnetostriction, and the magnetization process along the hard axis at 9 T can break the bulk single crystal.

Transport properties. The longitudinal and Hall resistivities were measured using a Quantum Design PPMS 9 with a standard four-probe method. The accuracy of the resistivity measurements was $\pm 5\%$. For room-temperature transport measurements, single crystals were cut to $17.10 \times 2.24 \times 1.16 \mu\text{m}^3$ using a focused ion beam to fix the samples without breaking them. High-field MR measurements were performed at the Dresden High Magnetic Field Laboratory using a pulsed magnet of 70 T.

First-principles calculations. We utilize first-principles calculations in the full-potential linearized augmented plane-wave code fleur (See <http://www.flapw.de>). Here, we use a plane-wave cut-off of 3.7 a.u.⁻¹ and a k -mesh of $16 \times 16 \times 7$ in the Brillouin zone. To reproduce the electronic structure and anisotropy effects²⁶ observed in experiments accurately, we utilize the GGA+U parameterization with $U = 4.0$ eV and $J = 0.97$ eV at the Mn atoms.

ARPES Measurements. Soft X-ray-ARPES measurements were performed at the SX-ARPES endstation³⁸ of the ADDRESS beamline³⁹ at the Swiss Light Source, Paul Scherrer Institute, Switzerland, using a SPECS analyzer. The increase of photoelectron mean free path in the soft-X-ray energy range results, by the Heisenberg uncertainty principle, in the high intrinsic resolution of the ARPES experiment in the out-of-plane momentum k_z ⁴⁰, allowing us to precisely locate electron states in the 3D Brillouin zone. The sample was cleaved in situ at 15 K with a base pressure lower than 1×10^{-10} mbar. The data were collected using circularly polarized light with an overall energy resolution of 50–80 meV. The photon energy is in the soft X-ray region (300–800 eV).

Data availability

The datasets generated and/or analyzed during the current study are available from the corresponding author on reasonable request.

Received: 4 February 2021; Accepted: 1 July 2021;

Published online: 28 July 2021

References

- Liu, E. et al. Giant anomalous Hall effect in a ferromagnetic kagome-lattice semimetal. *Nat. Phys.* **14**, 1125–1131 (2018).
- Sakai, A. et al. Giant anomalous Nernst effect and quantum-critical scaling in a ferromagnetic semimetal. *Nat. Phys.* **14**, 1119–1124 (2018).
- Potter, A., Kimchi, I. & Vishwanath, A. Quantum oscillations from surface Fermi arcs in Weyl and Dirac semimetals. *Nat. Commun.* **5**, 5161 (2014).
- Zhang, C. et al. Non-saturating quantum magnetization in Weyl semimetal TaAs. *Nat. Commun.* **10**, 1028 (2019).
- Ali, M. et al. Large, non-saturating magnetoresistance in WTe₂. *Nature* **514**, 205–208 (2014).
- Shekhar, C. et al. Extremely large magnetoresistance and ultrahigh mobility in the topological Weyl semimetal candidate NbP. *Nat. Phys.* **11**, 645–649 (2015).
- Huang, X. et al. Observation of the chiral-anomaly-induced negative magnetoresistance in 3D Weyl semimetal TaAs. *Phys. Rev. X* **5**, 031023 (2015).
- Ye, L. et al. Massive Dirac fermions in a ferromagnetic kagome metal. *Nature* **555**, 638–642 (2018).
- Manna, K., Muechler, L. & Kao, T. From colossal to zero: controlling the anomalous Hall effect in magnetic Heusler compounds via Berry curvature design. *Phys. Rev. X* **8**, 041045 (2018).
- Hu, J. & Rosenbaum, T. F. Classical and quantum routes to linear magnetoresistance. *Nat. Mater.* **7**, 697–700 (2008).
- Wang, S. X. & Li, G. Advances in giant magnetoresistance biosensors with magnetic nanoparticle tags: review and outlook. *IEEE Trans. Magn.* **44**, 1687–1702 (2008).
- Daughton, J. M. GMR applications. *J. Magn. Magn. Mater.* **192**, 334–342 (1999).
- Fullerton, E. E., Conover, M. J., Mattson, J. E., Sowers, C. H. & Bader, S. D. 150% magnetoresistance in sputtered Fe/Cr (100) superlattices. *Appl. Phys. Lett.* **63**, 1699–1701 (1993).
- Lin, C. et al. Spin correlations and colossal magnetoresistance in HgCr₂Se₄. *Phys. Rev. B* **94**, 224404 (2016).
- Jin, S. et al. Thousandfold change in resistivity in magnetoresistive La–Ca–Mn–O films. *Science* **264**, 413–415 (1994).
- Sinjukow, P. & Nolting, W. Metal-insulator transition in EuO. *Phys. Rev. B* **68**, 125107 (2003).
- Nagaev, E. L. Colossal-magnetoresistance materials: manganites and conventional ferromagnetic semiconductors. *Phys. Rep.* **346**, 387–531 (2001).

18. Yang, J. B. et al. Magnetic properties of the MnBi intermetallic compound. *Appl. Phys. Lett.* **79**, 1846–1848 (2001).
19. McGuire, M. A., Cao, H., Chakoumakos, B. C. & Sales, B. C. Symmetry-lowering lattice distortion at the spin reorientation in MnBi single crystals. *Phys. Rev. B* **90**, 174425 (2014).
20. Yang, J. B. et al. Structure and magnetic properties of the MnBi low temperature phase. *J. Appl. Phys.* **91**, 7866–7868 (2002).
21. Chen, X. H. et al. Correlation between the residual resistance ratio and magnetoresistance in MgB₂. *Phys. Rev. B* **65**, 024502 (2001).
22. Shiomi, Y., Onose, Y. & Tokura, Y. Extrinsic anomalous Hall effect in charge and heat transport in pure iron, Fe_{0.997}Si_{0.003}, and Fe_{0.97}Co_{0.03}. *Phys. Rev. B* **79**, 100404(R) (2009).
23. Baily, S. A. & Salamon, M. B. Berry-phase contribution to the anomalous Hall effect in gadolinium. *Phys. Rev. B* **71**, 104407 (2005).
24. Angadi, M. A. & Thanigaimani, V. Hall effect in MnBi thin films. *J. Mater. Sci. Lett.* **7**, 717–721 (1988).
25. Nagaosa, N., Sinova, J., Onoda, S., MacDonald, A. H. & Ong, N. P. Anomalous Hall effect. *Rev. Mod. Phys.* **82**, 1539 (2010).
26. Antropov, V. P., Antonov, V. N., Bekenov, L. V., Kutepov, A. & Kotliar, G. Magnetic anisotropic effects and electronic correlations in MnBi ferromagnet. *Phys. Rev. B* **90**, 054404 (2014).
27. Choi, Y. et al. Element-resolved magnetism across the temperature- and pressure-induced spin reorientation in MnBi. *Phys. Rev. B* **94**, 184433 (2016).
28. Coehoorn, R. & De Groot, R. A. The electronic structure of MnBi. *J. Phys. F* **15**, 2135 (1985).
29. Kharel, P. et al. Transport spin polarization of high Curie temperature MnBi films. *Phys. Rev. B* **83**, 024415 (2011).
30. Hiruma, K. & Miura, N. Magnetoresistance study of Bi and Bi–Sb alloys in high magnetic fields. II. Landau levels and semimetal-semiconductor transition. *J. Phys. Soc. Japan* **52**, 2118–2127 (1983).
31. Kumar, N. et al. Observation of pseudo-two-dimensional electron transport in the rock salt-type topological semimetal LaBi. *Phys. Rev. B* **93**, 241106 (2016).
32. Hirschberger, M. et al. The chiral anomaly and thermopower of Weyl fermions in the half-Heusler GdPtBi. *Nat. Mater.* **15**, 1161–1165 (2016).
33. Qu, D. X., Hor, Y. S., Xiong, J., Cava, R. J. & Ong, N. P. Quantum oscillations and Hall anomaly of surface states in the topological insulator Bi₂Te₃. *Science* **329**, 821–824 (2010).
34. He, B. et al. Magnon-induced giant anomalous Nernst effect in single crystal MnBi. Preprint at *arXiv* <https://arxiv.org/abs/2009.02211> (2020).
35. Nakatsuji, S., Kiyohara, N. & Higo, T. Large anomalous Hall effect in a non-collinear antiferromagnet at room temperature. *Nature* **527**, 212–215 (2015).
36. Masuda, H. et al. Quantum Hall effect in a bulk antiferromagnet EuMnBi₂ with magnetically confined two-dimensional Dirac fermions. *Sci. Adv.* **2**, e1501117 (2016).
37. Deng, Y. et al. Quantum anomalous Hall effect in intrinsic magnetic topological insulator MnBi₂Te₄. *Science* **367**, 895–900 (2020).
38. Strocov, V. N. et al. Soft-X-ray ARPES facility at the ADDRESS beamline of the SLS: Concepts, technical realisation and scientific applications. *J. Synchrotron Radiat.* **21**, 32 (2014).
39. Strocov, V. N. et al. High-resolution soft X-ray beamline ADDRESS at the Swiss Light Source for resonant inelastic X-ray scattering and angle-resolved photoelectron spectroscopies. *J. Synchrotron Radiat.* **17**, 631 (2010).
40. Strocov, V. N. et al. Three-dimensional electron realm in VSe₂ by soft-X-ray photoelectron spectroscopy: origin of charge-density waves. *Phys. Rev. Lett.* **109**, 086401 (2012).
41. Selmi, A., Gibart, P. & Goldstein, L. Galvanomagnetic properties of n-type ferromagnetic semiconductor HgCr₂Se₄. *J. Magn. Magn. Mater.* **15**, 1285–1286 (1980).
42. Wang, Y. et al. Anisotropic anomalous Hall effect in triangular itinerant ferromagnet Fe₃GeTe₂. *Phys. Rev. B* **96**, 134428 (2017).
43. Dijkstra, J., ijlema, P. J., Van Bruggen, C. F., Haas, C. & De Groot, R. A. Band-structure calculations of Fe_{1/3}Ta₂S₂ and Mn_{1/3}Ta₂S₂, and transport and magnetic properties of Fe_{0.28}Ta₂S₂. *J. Phys. Condens. Matter* **1**, 6363 (1989).
44. Mooodera, J. S. & Mootoo, D. M. Nature of half-metallic ferromagnets: Transport studies. *J. Appl. Phys.* **76**, 6101–6103 (1994).
45. Wang, Y. et al. Magnetic anisotropy and topological Hall effect in the trigonal chromium tellurides Cr₅Te₈. *Phys. Rev. B* **100**, 024434 (2019).

Acknowledgements

This study was financially supported by an Advanced Grant from the European Research Council (No. 742068) “TOPMAT”, the European Union’s Horizon 2020 research and innovation program (No. 824123) “SKYTOP”, the European Union’s Horizon 2020 research and innovation program (No. 766566) “ASPIN”, the Deutsche Forschungsgemeinschaft (Project-ID 258499086) “SFB 1143”, the Deutsche Forschungsgemeinschaft (Project-ID FE 633/30-1) “SPP Skyrmions”, and the DFG through the Würzburg-Dresden Cluster of Excellence on Complexity and Topology in Quantum Matter ct.qmat (EXC 2147, Project-ID 39085490). We acknowledge the support of the Dresden High Magnetic Field Laboratory (HLD) at HZDR and members of the European Magnetic Field Laboratory (EMFL).

Author contributions

Y.H. and C.F. conceived this work. The single crystals were grown by Y.H. The crystal, magnetic, and transport measurements were characterized by Y.H. with the help of T.H., T.R., W.S., and M.N. The FIB microstructure transport devices were fabricated by T.H., J.G., and Y.S., and G.H.F. provided the theoretical support. The ARPES measurements were conducted by M.Y. and supported by V.N.S. All the authors discussed the results. The manuscript was written by Y.H. and G.H.F., with feedback from all the authors. The project was supervised by C.F.

Funding

Open Access funding enabled and organized by Projekt DEAL.

Competing interests

The authors declare no competing interests.

Additional information


Supplementary information The online version contains supplementary material available at <https://doi.org/10.1038/s41467-021-24692-7>.

Correspondence and requests for materials should be addressed to Y.H.

Peer review information *Nature Communications* thanks the anonymous reviewer(s) for their contribution to the peer review of this work. Peer reviewer reports are available.

Reprints and permission information is available at <http://www.nature.com/reprints>

Publisher’s note Springer Nature remains neutral with regard to jurisdictional claims in published maps and institutional affiliations.

 **Open Access** This article is licensed under a Creative Commons Attribution 4.0 International License, which permits use, sharing, adaptation, distribution and reproduction in any medium or format, as long as you give appropriate credit to the original author(s) and the source, provide a link to the Creative Commons license, and indicate if changes were made. The images or other third party material in this article are included in the article’s Creative Commons license, unless indicated otherwise in a credit line to the material. If material is not included in the article’s Creative Commons license and your intended use is not permitted by statutory regulation or exceeds the permitted use, you will need to obtain permission directly from the copyright holder. To view a copy of this license, visit <http://creativecommons.org/licenses/by/4.0/>.

© The Author(s) 2021